iScience

CellPress
OPEN ACCESS

Article

# Ganglioside lipidomics of CNS myelination using direct infusion shotgun mass spectrometry

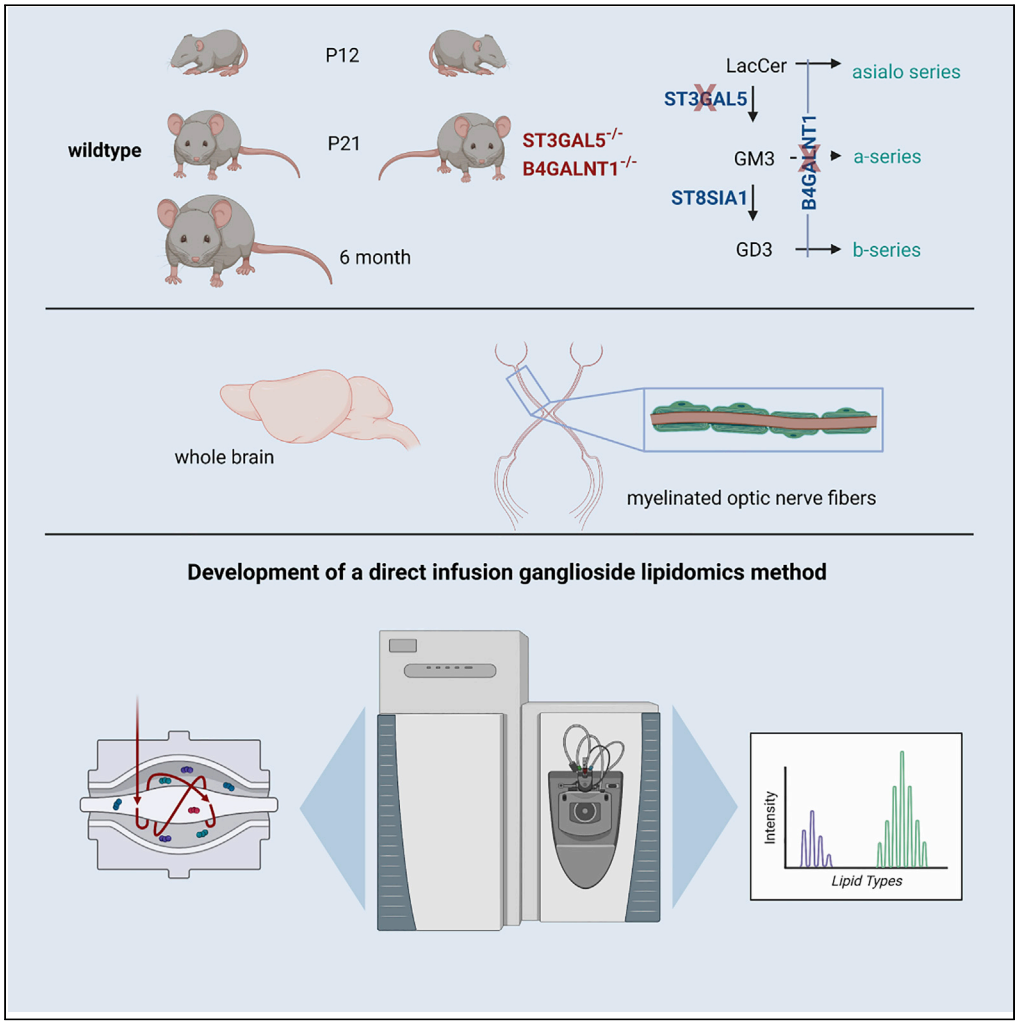


Martina Arends, Melanie Weber, Cyrus Papan, ..., Martina Schifferer, Christian Klose, Mikael Simons

klose@lipotype.com (C.K.)
mikael.simons@dzne.de (M.S.)

## Highlights

A sensitive direct infusion mass spectrometry method for ganglioside lipidomics

Quantification of gangliosides in CNS myelin development

Generation of myelin in the absence of gangliosides

Arends et al., iScience 25, 105323
November 18, 2022 
https://doi.org/10.1016/j.isci.2022.105323

iScience

CellPress
OPEN ACCESS

Article

# Ganglioside lipidomics of CNS myelination using direct infusion shotgun mass spectrometry

Martina Arends,[1,2] Melanie Weber,[3] Cyrus Papan,[3] Markus Damm,[3] Michal A. Surma,[3] Christopher Spiegel,[3] Minou Djannatian,[1,2] Shengrong Li,[4] Lisa Connell,[4] Ludger Johannes,[5] Martina Schifferer,[1,2,6] Christian Klose,[3,*] and Mikael Simons[1,2,6,7,8,*]

## SUMMARY

**Gangliosides are present and concentrated in axons and implicated in axon-myelin interactions, but how ganglioside composition changes during myelin formation is not known. Here, we present a direct infusion (shotgun) lipidomics method to analyze gangliosides in small amounts of tissue reproducibly and with high sensitivity. We resolve the mouse ganglioside lipidome during development and adulthood and determine the ganglioside content of mice lacking the *St3gal5* and *B4galnt1* genes that synthesize most ganglioside species. Our results reveal substantial changes in the ganglioside lipidome during the formation of myelinated nerve fibers. In sum, we provide insights into the CNS ganglioside lipidome with a quantitative and sensitive mass spectrometry method. Since this method is compatible with global lipidomic profiling, it will provide insights into ganglioside function in physiology and pathology.**

## INTRODUCTION

Information processing in complex organisms requires the formation of myelin. Myelin is generated in the CNS by oligodendrocytes wrapping their plasma membrane in multiple layers around an axon. Myelin segments are typically arranged in regular distances on the axons and separated by narrow gaps, the nodes of Ranvier, which contain the voltage-gated sodium channels that are required for fast and efficient nerve conduction (Stadelmann et al., 2019; Simons and Nave, 2015). The myelin sheath is attached to the axon at each end of an internode where the myelin membrane forms paranodal loops, held together by adhesion proteins (Rasband and Peles, 2015). We have previously shown that myelin grows by the movement of the innermost layer of myelin around the axonal membrane together with the lateral extension of the individual layers of myelin along the axon toward the future node (Snaidero et al., 2014; Djannatian et al., 2019). For this mode of myelin growth, continuous actin filament turnover wraps newly generated myelin sheaths around the axon (Zuchero et al., 2015; Nawaz et al., 2015). The movement of one plasma membrane around another is unusual as membranes are in general repulsive and adhesive forces are necessary to fix the growing myelin sheath to the axonal surface, raising the question of the molecules involved (Bakhti et al., 2013). Candidate molecules are gangliosides, which are present and concentrated on axons (Schnaar et al., 2014; Olsen and Faergeman, 2017). There are several previous observations suggesting a role of gangliosides in the biogenesis of myelinated nerves (Schnaar et al., 2014; Sheikh et al., 1999; Ma et al., 2003). Gangliosides are present and concentrated in axons (Olsen and Faergeman, 2017) with some gangliosides (GM1) being specifically enriched in white matter tracts. In fact, brain ganglioside synthesis and myelination overlap temporally (Molander et al., 2000; Vajn et al., 2013). Finally, one adhesion molecule located at the axon-myelin interface, the myelin-associated glycoprotein, MAG, binds to GD1a and GT1b (Pronker et al., 2016; Collins et al., 1997, 1999; Yang et al., 1996). Most importantly, double knockout mice that lack the St3Gal5 gene (encoding GM3 synthase) and the B4galnt1 gene (encoding GM2 synthase) are unable to synthesize significant amounts of brain gangliosides and develop axonal degeneration and perturbed axon-glia interactions (Yamashita et al., 2005). On this basis, we assumed that the coalescence of ganglioside domains on the axonal surface might form a permissive and rigid substrate for myelin membrane wrapping.

Gangliosides display a high degree of structural heterogeneity, creating a large group of ganglioside species. The synthesis is a developmentally regulated, region-dependent, and stepwise process (Figure 1) (Desplats et al., 2007; Kolter et al., 2002). Glycosphingolipid precursors are synthesized in the endoplasmic

[1]Institute of Neuronal Cell Biology, Technical University Munich, 80802 Munich, Germany

[2]German Center for Neurodegenerative Diseases (DZNE), 81377 Munich, Germany

[3]Lipotype, 01307 Dresden, Germany

[4]Avanti Lipids, 35007 Alabama, USA

[5]Institut Curie, Université PSL, U1143 INSERM, UMR3666 CNRS, 75248 Paris, France

[6]Munich Cluster of Systems Neurology (SyNergy), 81377 Munich, Germany

[7]Institute for Stroke and Dementia Research, University Hospital of Munich, LMU Munich, 81377 Munich, Germany

[8]Lead contact

*Correspondence: klose@lipotype.com (C.K.), mikael.simons@dzne.de (M.S.)

https://doi.org/10.1016/j.isci.2022.105323

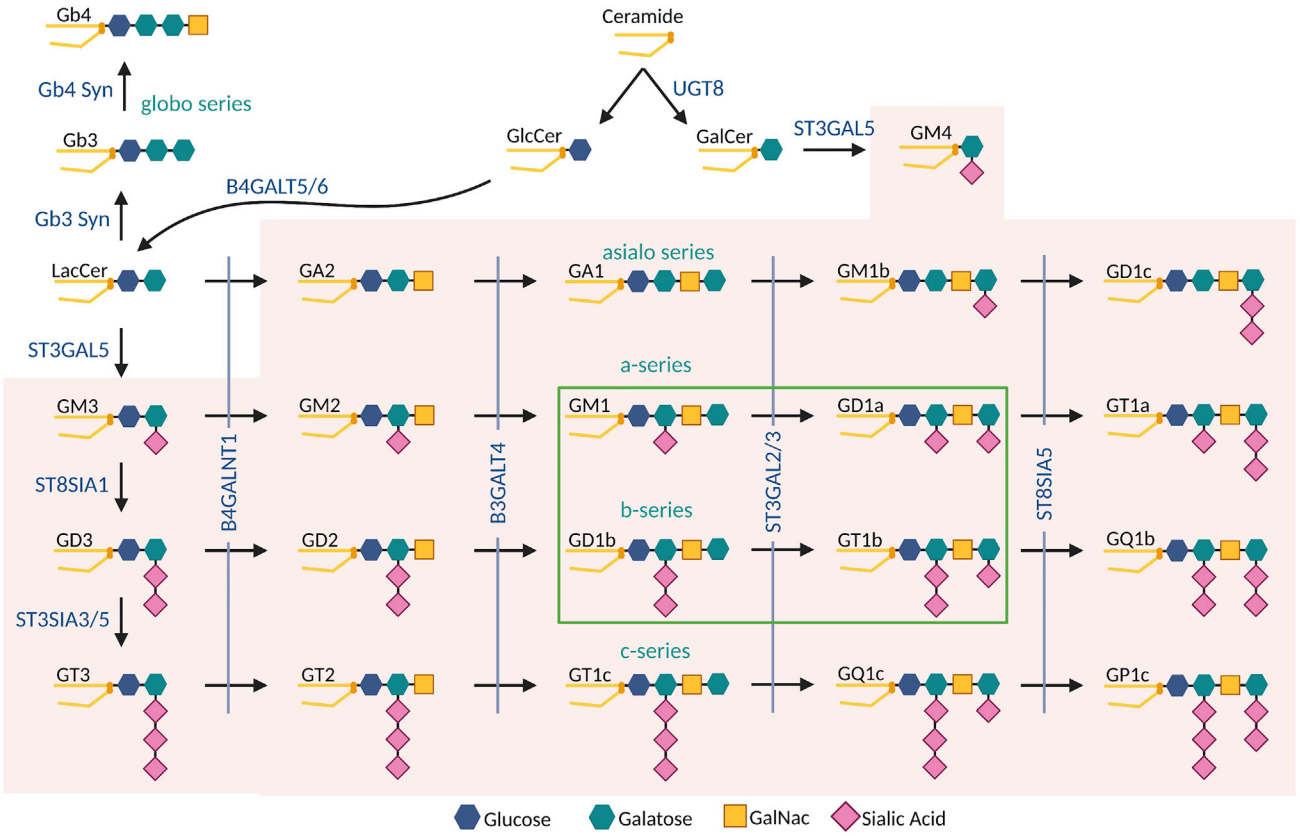


**Figure 1. Ganglioside synthesis pathway**

Synthesis of gangliosides of the asialo, a-, b-, and c-series is shown. All gangliosides are synthesized from ceramide by the addition of sugar groups and sialic acid. Gangliosides that are not synthesized anymore in *St3gal5/B4galnt1*-deficient mice are highlighted in red. Major brain gangliosides are encircled in green.

reticulum followed by glycosylation of ceramide in the Golgi apparatus, resulting in glucosylceramide (GlcCer) (Futerman and Pagano, 1991; Hirschberg et al., 1993; Lahiri and Futerman, 2007), which is further transformed into lactosylceramide (LacCer), the metabolic substrate for the synthesis of all complex glycosphingolipids. The simplest ganglioside species GM3 contains a single sialic acid. With further development, more complex gangliosides are being synthesized by the addition of glycans and more sialic acids (Kolter et al., 2002; Lahiri and Futerman, 2007; Russo et al., 2018). In rat brains, simple gangliosides like GD3 and GM3 are predominantly found at early embryonic stages (E14) (Yu et al., 1988; Irwin et al., 1980), whereas the more complex gangliosides, GM1, GD1a, and GT1b, increase from E18 onward. The general functions of gangliosides have been examined by analyzing mouse mutants that lack enzymes required for distinct steps in their synthesis. These studies have revealed a high degree of redundancy and/or functional compensation (Yamashita et al., 2003; Sturgill et al., 2012). For example, mice that only lack GM3 synthase (*St3gal5* deficient mice) are still able to synthesize 0-series gangliosides abundantly and are only characterized by a higher sensitivity to insulin and by hearing loss (Yamashita et al., 2003; Yoshikawa et al., 2009). Mice deficient in *B4galnt1*, the gene encoding for GM2/GD2 synthase, cannot synthesize gangliosides of higher complexity, yet they are born normally and show only slight neurological deficits from 10 weeks after birth characterized by a reduction of conduction velocity (Takamiya et al., 1996; Liu et al., 1999; Susuki et al., 2007). Ultrastructural analysis at later ages revealed paranodal deficits with enlarged and disorganized loops and Wallerian-like degeneration in CNS and PNS (McGonigal et al., 2019; Sheikh et al., 1999; Ma et al., 2003; Susuki et al., 2007). In contrast, mice deficient in both *St3gal5* and *B4galnt1* genes, that lack all gangliosides, are severely impaired (Yamashita et al., 2005). Double mutant mice are born with a seemingly normal nervous system. However, they develop severe neurological deficits and die within 1-3 months. Structural and ultrastructural analysis of 1.5- to 3-month-old double mutant mice displayed white matter vacuolization, axonal degeneration, and disorganized paranodes in the CNS.

While these studies indicate the role of gangliosides in maintaining functional myelinated axons, an analysis of their role at the early stages of myelination is lacking. Here, we analyzed mouse brain and optic nerve samples to study the role of gangliosides in myelination. To do so, we developed a mass spectrometry analysis method allowing the quantification of ganglioside levels during myelination in low amounts of tissue.

## RESULTS

### A mass spectrometry method to analyze the ganglioside lipidome

Quantitative analysis of gangliosides is usually performed by liquid chromatography-mass spectrometry (LC-MS), and several methods, including their validation, have been published (Fong et al., 2009; Ikeda et al., 2008; Wormwood Moser et al., 2021; Horejsi et al., 2021). Common methodological themes in the analysis of gangliosides are the canonical Svennerholm extraction (Svennerholm and Fredman, 1980) and enrichment of the analytes by C18-silica solid-phase extraction (SPE) (Williams and McCluer, 1980). These methods exhibit satisfying sensitivity and reproducibility. Additionally, they even allow for the discrimination of isomeric ganglioside species. However, LC-MS-based approaches to the analysis of gangliosides require relatively large sample amounts and demand dedicated, often time-consuming extraction and enrichment procedures. For example, the analysis of mouse brain homogenate requires about 0.5 g wet weight of tissue, and extraction is done in 15-20 mL of organic solvents (Ikeda et al., 2008). Both sample amount and extraction volume render this approach unsuitable for high-throughput lipidomic analysis of gangliosides. Additionally, the need for large sample amounts prevents the analysis of small anatomical structures, such as the mouse optic nerve.

To overcome these limitations, we developed a direct infusion (shotgun) lipidomics method requiring only a few hundred μg of tissue material and extraction volumes <2 mL. In brief, tissue homogenates were extracted using a 2-step chloroform/methanol procedure to recover neutral (triglycerides and cholesterol esters) as well as polar lipids (mainly phospholipids) by using an automated liquid handling device as described previously (Surma et al., 2015, 2021). From the remaining water phase, the acidic glycosphingolipids (gangliosides) were subsequently enriched based on SPE in a 96-well format. Gangliosides were eluted and infused into the mass spectrometer with a robotic nano-electrospray ionization device (for method details see STAR methods).

The newly developed shotgun lipidomics method for the analysis of gangliosides was validated using wild-type mouse brain homogenates (Figure S1; Tables S1 and S2). Brain-tissue titration revealed that species belonging to the major mouse brain ganglioside classes (GM1, GD1, GT1, and GQ1) can be detected starting from 50 μg of tissue, and the signal increases linearly until 1000 μg of tissue. Species coverage agrees with previous reports for the major ganglioside classes, and 36:1; 2 and 38:1; 2 are the most abundant species. Species with carbon chain length >38 as well as O-acetylated gangliosides could be detected at minor amounts. Additionally, minor amounts of GM3, GD3, and GD2 could be detected. The limit of detection (LOD) and limit of quantification (LOQ) calculated based on the titration of ganglioside reference standards were around 10 and 20 nM, respectively (the actual values depend on the ganglioside class, see Table S2). Linearity was achieved across four orders of magnitude. Method reproducibility as assessed by the repeated analysis (n = 3) of aliquots of pooled mouse brain homogenate was satisfactory: 14% (relative SD, RSD) for lipid classes for which an internal standard was available (GM1), and 22.3% for lipid classes for which no internal standard was available (GD1, GT1, and GQ1).

### The brain and optic nerve lipidome during mouse development

To assess how the lipid composition changes during developmental myelination, we analyzed mouse brains at an early stage of myelination (P12), at a stage when myelination is ongoing, but almost completed (P21), and at an adult stage (6 months), when developmental myelination is fully completed. Lipidomic data were normalized to internal standards to determine the absolute quantity of lipid species; subsequently, data were transformed to mol % per sample for each lipid. A principal component analysis (PCA) shows that the biological replicates clustered together demonstrating technical and biological reproducibility of the samples (Figures 1 and 2A). Multivariate statistical data analysis was applied to evaluate the variations in the lipidomes.

Using our method, we determined the levels of gangliosides in the mouse brain during development normalized to GM1 standard and to total lipids for each sample (Figure 2B). By far the highest amounts

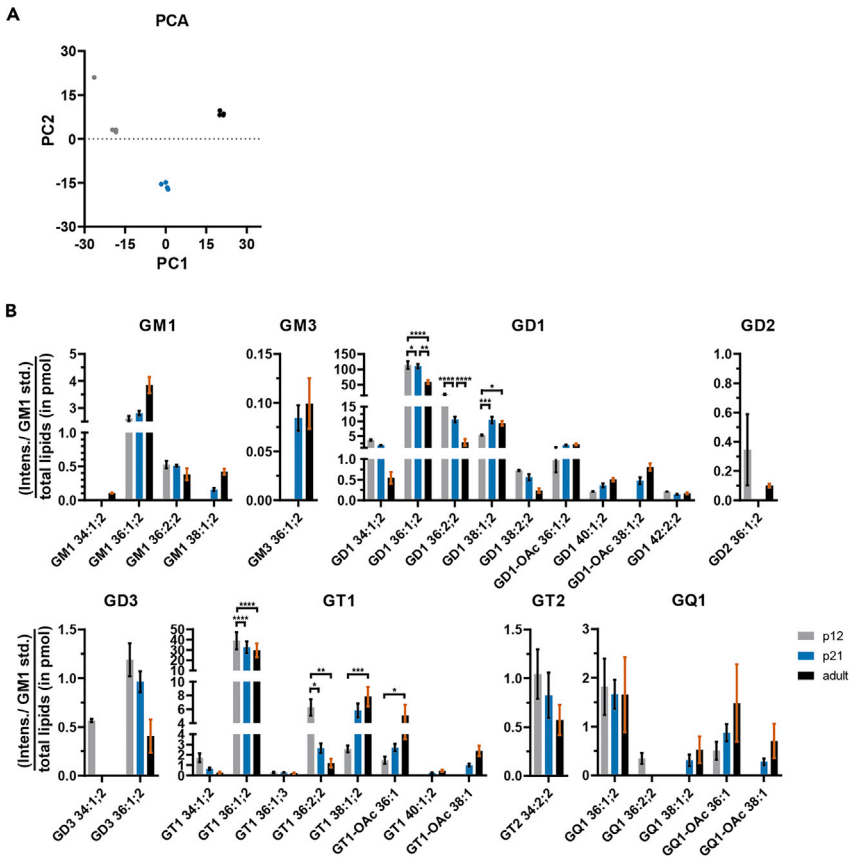


**Figure 2. Developmental change of ganglioside content in the brain of wild-type mice at P12, P21, and 6 months (adult)**

(A) PCA shows clustering of biological replicates for every age. The lipid species' percentage of moles per age was used as input data.

(B) Ganglioside composition. Intensities are normalized to GM1 standard and then to total lipid amounts. Graphs represent mean values. n = 4 for every age. All values are represented as mean ± SD. Abbreviations: Lipid classes as defined by Lipid Maps Classification. See also Tables S1, S2, and S3; Figures S1 and S2.

were detected in GD1 species, followed by GT1. We found lower amounts of GM1 and GQ1, while the levels of GD3, GT2, GD2, and GM3 were among the lowest. Some species of lower complexity (e.g. GD2, GD3, and GT2) were abundant at P12 and P21. Of the more complex ganglioside classes (e.g. GD1 and GT1), species with longer carbon chains and more double bonds are preferentially expressed at the adult stage. This holds true, especially for O-acetylated species. The most abundant gangliosides were GD1 36:1; 2 and GT1 36:1; 2 at P12 and adult age. GD1 36:2; 2 was among the most abundant gangliosides at P12. However, their amount decreased significantly during development.

Next, we determined the optic nerve lipid composition at P12, P21, and the adult stage (6 months). We used the optic nerves of young mice to show that our newly developed method is also applicable on small amounts of tissue. Additionally, optic nerves consist mainly of axons and cells of the oligodendrocyte lineage; hence, by using optic nerves, the number of gangliosides will be lowered to those that are involved in axo-glial processes. The PCA of the optic nerve also shows that the biological replicates clustered together demonstrating the technical and biological reproducibility of the samples (Figure 3A).

We also determined the levels of gangliosides normalized to GM1 standard and to total lipids for each sample in the optic nerve during development (Figure 3B). Similar to the brain samples, the highest amounts of gangliosides were detected in the GD1 and GT1 class, with GD1 36:1; 2 and GT1 36:1; 2 being

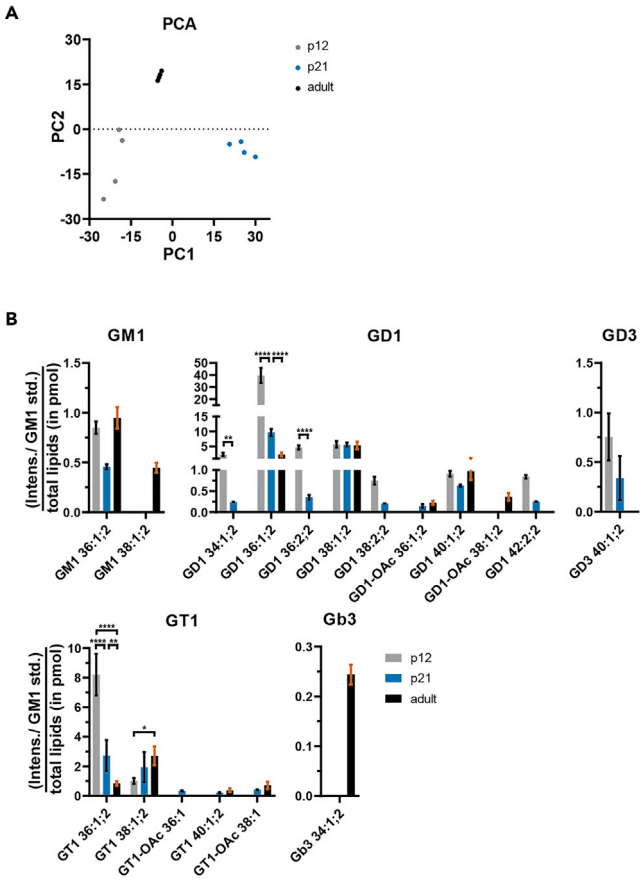


**Figure 3. Developmental change of ganglioside content in the optic nerve of wild-type mice at P12, P21, and 6 months (adult)**

(A) PCA shows clustering of biological replicates for every age. The lipid species' percentage of moles per age was used as input data.

(B) Ganglioside composition. Intensities are normalized to GM1 standard and then to total lipid amounts. Graphs represent mean values. n = 4 for every age. All values are represented as mean ± SD. Abbreviations: Lipid classes as defined by Lipid Maps Classification. See also Tables S1 and S3; Figure S3.

the most abundant species at P12 with all of them significantly decreasing during development. Interestingly, at adult age, GD1 38:1; 2 and GT1 38:1; 2 become the most abundant ganglioside species in the mouse optic nerve. GM3, GD2, GT2, and GQ1 were not detected in murine optic nerves, and the amounts of GM1 were much lower than in brain samples. While GD3 was not found at adult age, Gb3 was found only at this age. Within the ganglioside classes, both shorter carbon chains and the lower number of double bonds were found at P12 and P21, whereas species with longer carbon chains and/or more double bonds dominated at the adult stage.

Additionally, we determined the levels of other lipid classes as the molar percentage of the total lipid amount. Lipid class levels for brain samples are shown in Figure S1A and for optic nerves in Figure S2A. We measured a huge increase in hexosylceramide (HexCer), especially from P12 to P21 in the brain samples. In the brain samples, the amount of lysophospholipids increases from P12 to P21 and decreases from P21 to the adult stage, whereas in the optic nerve samples, lysophospholipids constantly decrease. The amounts of sulfatides (Sulf), sphingomyelin (SM), diacylglycerol (DAG), and cholesterol (Chol) increase during development in both sample types, while phosphatidylcholine (PC) and ceramide (Cer) levels constantly decrease. We determined the average length and the number of double bonds of the carbon chains of each lipid class in both sample types (Figures S2, S3B, and S3C). In general, we observed an increasing length of the carbon chains and an increasing number of double bonds during development.

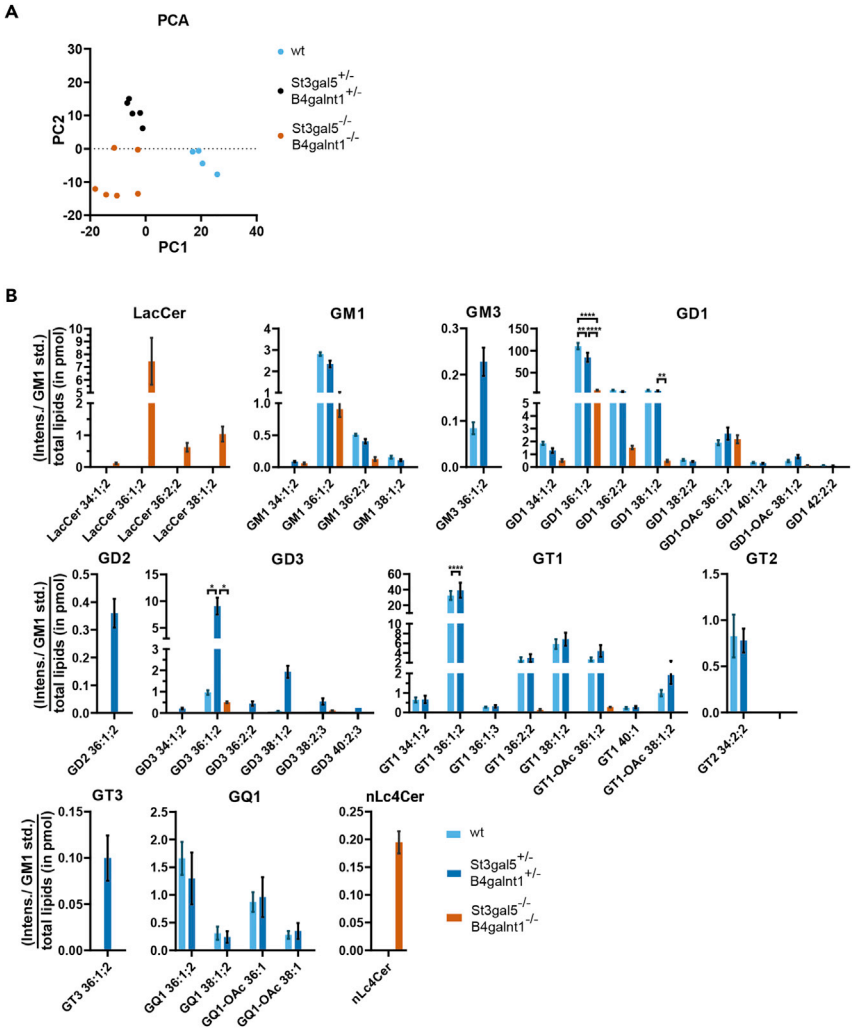


**Figure 4. Comparison of the gangliosides distribution in the brain of P21 *St3gal5/B4galnt1*-deficient mice with *St3gal5/B4galnt1* double heterozygous and wild-type animals**

(A) PCA shows clustering of wild-type and *St3gal5*$^{+/}$*/B4galnt1*$^{+/-}$ samples, whereas the samples of *St3gal5*$^{-/-}$*/B4galnt1*$^{-/-}$ mice spread in both dimensions. The lipid species' percentage of moles per genotype was used as input data.

(B) Ganglioside composition. Intensities for each genotype are normalized to GM1 standard and then to total lipid amounts. Graphs represent mean values. n = 3 for *St3gal5*$^{+/}$*/B4galnt1*$^{+/-}$ and *St3gal5*$^{-/-}$*/B4galnt1*$^{-/-}$ samples and n = 4 for wild-type samples. All values are represented as mean ± SD. Abbreviations: Lipid classes as defined by Lipid Maps Classification. See also Tables S1 and S3; Figure S4.

## Ganglioside lipidomics of *St3gal5/B4galnt1*-deficient mouse brains and optic nerves

To determine the lipid composition in the brain and optic nerve of ganglioside-deficient mice, we cross-bred mice deficient in *St3gal5* and *B4galnt1*, to obtain double heterozygous and *St3gal5/B4galnt1*-deficient mice, which we compared to wild-type mice at P21. *St3gal5/B4galnt1*-deficient mice lack the enzymes to metabolize LacCer into gangliosides. The PCA shows that brain samples from double heterozygous and wild-type samples cluster together, while *St3gal5/B4galnt1*-deficient replicates segregated and spread slightly in both dimensions (Figure 4A).

We determined the levels of gangliosides normalized to GM1 standard and then to total lipids in pmol for each sample in the brain of the *St3gal5/B4galnt1*-deficient and heterozygous mice (Figure 4B). All gangliosides are synthesized from LacCer, and we found, as expected, high levels of LacCer in all replicates of *St3gal5/B4galnt1*-deficient mice, whereas it was not detectable in wild-type or double heterozygous samples. Among the detected gangliosides, GD1 and GT1 were measured in the highest amounts. The

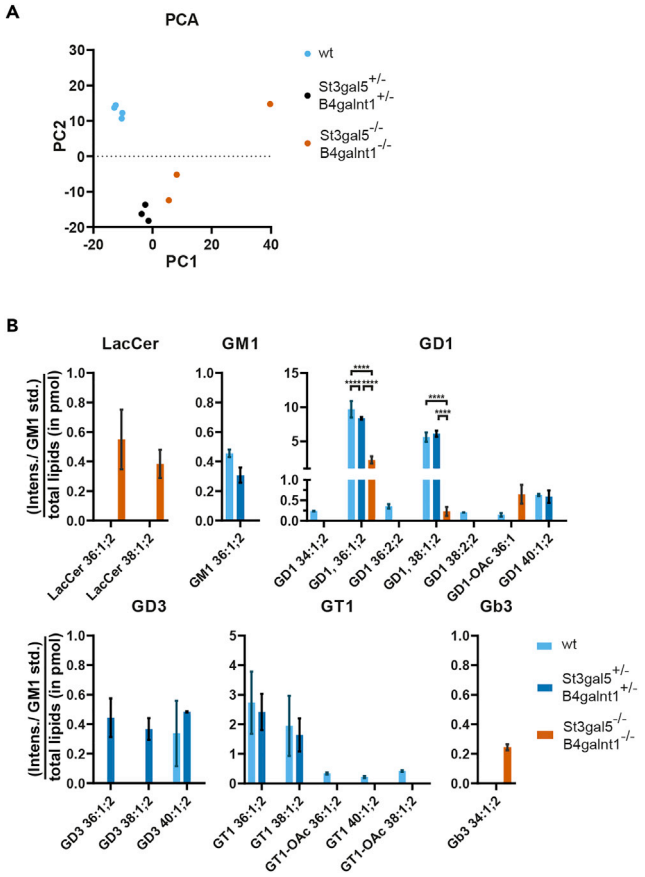


**Figure 5. Comparison of the gangliosides and lipid class distribution in the optic nerve of P21 *St3gal5/B4galnt1*-deficient mice with double heterozygous and wild-type**

(A) PCA shows clustering of each, wild-type and *St3gal5*$^{+/}$/*B4galnt1*$^{+/-}$ samples, whereas the samples of *St3gal5*$^{-/-}$/*B4galnt1*$^{-/-}$ mice spread in both dimensions. The lipid species' percentage of moles per genotype was used as input data.

(B) Ganglioside composition. Intensities for each genotype are normalized to GM1 and then to total lipid amounts. Graphs represent mean values. n = 3 for *St3gal5*$^{+/}$/*B4galnt1*$^{+/-}$ and *St3gal5*$^{-/-}$/*B4galnt1*$^{-/-}$ samples and n = 4 for wild-type samples. All values are represented as mean ± SD. Abbreviations: Lipid classes as defined by Lipid Maps Classification. See also Tables S1 and S3; Figure S5.

ganglioside classes GM1, GD1, GT1, GT2, and GQ1 showed similar amounts in wild-type and double heterozygous mice, while we detected much higher amounts in *St3gal5/B4galnt1*-deficient samples for GD2 and GD3. GT3 was detected in double heterozygous samples only. As expected from the work of Yamashita et al., 2005, we detected weak signals for GM1, GD1, and GD3 signals in double knockout animals. They found that this was due to sialylated neolacto-series glycosphingolipids. In line with their findings, we detected a signal in *St3gal5/B4galnt1*-deficient mice for nLc4-Cer (Figure 4).

Next, we investigated the composition of lipids and gangliosides in the optic nerves of *St3gal5/B4galnt1*-deficient mice. The PCA showed that samples from double heterozygous and wild-type samples cluster together, while *St3gal5/B4galnt1*-deficient replicates segregated and spread in both dimensions (Figure 5A). When we measured the levels of gangliosides normalized to GM1 standard and then to total lipids in pmol for each sample in optic nerve samples of the double heterozygous and *St3gal5/B4galnt1*-deficient samples, we found GD1 and GT1 in the highest levels again with similar amounts in wild-type and double heterozygous samples (Figure 5B). GM1 and GD3 were detected in lower amounts. We also found residual amounts of GM1, GD1, and GD3 in the *St3gal5/B4galnt1*-deficient mice. However, as demonstrated by Yamashita et al., 2005, these signals are most likely from sialylated neolacto-series glycosphingolipids. As it was expected, LacCer was found in *St3gal5/B4galnt1*-deficient samples only. The lipid levels of all other

lipid classes as the percentage of the total lipid amount for each sample do not indicate a big difference in double heterozygous or *St3gal5/B4galnt1*-deficient mice compared to wild-type animals, neither in the brain samples nor in the optic nerve samples (Figures S4A and S5A). Significantly, different levels were only detected within the glycerophospholipids (GPLs), whereas PS levels increased in both double heterozygous and double knockout samples in the brain and optic nerve samples. In the optic nerve, the PE levels of double heterozygous and double knockout samples were reduced. Though not significant, we observed a decrease in SM levels in brain samples and DAG levels in optic nerve samples. Neither the average carbon chain length nor the average number of double bonds is changed significantly in the brain samples of double heterozygous and *St3gal5/B4galnt1*-deficient mice compared to wild-type mice (Figures S4B and S4C). The same holds true for carbon chains and the number of double bonds in the optic nerve samples (Figures S5B and S5C). However, the average length of sulfatide carbon chains in optic nerve samples increases in *St3gal5/B4galnt1*-deficient mice compared to wild-type mice, while the average length of SM carbon chains decreases. In addition, the number of double bonds decreases in SM as well as in DAG.

### Hypomyelination in the optic nerve of *St3gal5/B4galnt1*-deficient mice

Next, we analyzed myelination in the optic nerve of *St3gal5/B4galnt1*-deficient mice. Previous work has shown that *St3gal5/B4galnt1*-deficient mice develop severe neurological deficits and die within 1-3 months. Structural and ultrastructural analysis of 1.5- to 3-month-old double-mutant mice displayed white matter vacuolization, axonal degeneration, and disorganized paranodes in the CNS (Yamashita et al., 2005), but whether the phenotype is a result of myelin degeneration or impaired myelin formation is not known.

As described previously, *St3gal5/B4galnt1*-deficient mice were of small size and developed severe motor impairment. They reached their clinical endpoint already at ~ P21 and could therefore not be analyzed at later developmental stages. We used electron microscopy to analyze the ultrastructure of myelin in the optic nerve of *St3gal5/B4galnt1*-deficient mice at P12, an early stage of myelination, and P21, a stage where myelination is almost completed. Myelination was surprisingly normal with no obvious abnormal myelin profiles such as outfoldings or double myelination profiles (Figure 6A). At P12, we did not observe a difference in the number of axons being myelinated between *St3gal5/B4galnt1*-deficient mice and their double heterozygous littermates (Figure 6B). At P21, we detected a small reduction of myelinated axons in *St3gal5/B4galnt1*-deficient mice ($p = 0.045$). To determine myelin thickness, we performed g ratio measurements (the ratio of the inner axonal diameter to the total outer diameter), which showed slightly thinner myelin sheaths and a higher g ratio in *St3gal5/B4galnt1*-deficient mice (g ratio = 0.77) than in their double heterozygous littermates (g ratio = 0.71) (Figures 6C and 6D). Next, we assessed the ultrastructure of the paranodal region at P12 and P21. There was no difference in the number of loops per paranode or the nodal length per axonal diameter (Figures S5A, S5B, and S5D). Nevertheless, the paranodal length per axonal diameter at P21 appeared smaller ($p = 0.06$), and we counted more detached paranodal loops at P12 and P21 in *St3gal5/B4galnt1*-deficient mice ($p = 0.13$ and $p = 0.07$) (Figures S6C and S6E). Thus, we conclude that gangliosides play only a minor role in myelin biogenesis. The white matter vacuolization profiles observed previously in 1.5- to 3-month-old *St3gal5/B4galnt1*-deficient mice (Yamashita et al., 2005) are most likely a result of impaired maintenance and/or increased degeneration.

## DISCUSSION

Our understanding of gangliosides and their functions within the CNS has been difficult to elucidate due to the limitations of current analytical methods. While thin-layer chromatography is an appropriate method to detect different ganglioside classes, this method is limited in precisely quantifying ganglioside content, discriminating isomers, and detecting differences in the ceramide moiety. Recent advances in mass spectrometry analysis account for more sensitive and precise glycosphingolipid detection in samples (reviewed in Barrientos and Zhang, 2020). Typically, analytical methods for the analysis of glycosphingolipids are characterized by dedicated extraction protocols, the requirements for rather high sample amounts (up to several hundred mg), resulting in the need of large volumes of organic solvents for lipid extraction (>10 mL), an alkaline hydrolysis step to remove glycerol(phospho)lipids, and sometimes extended analysis times due to long chromatographic gradients (up to 30 min) prior to mass spectrometric analysis (Fong et al., 2009; Ikeda et al., 2008; Horejsi et al., 2021; Barrientos and Zhang, 2020; Wormwood Moser et al., 2021) (Panzenboeck et al., 2020). While these methods

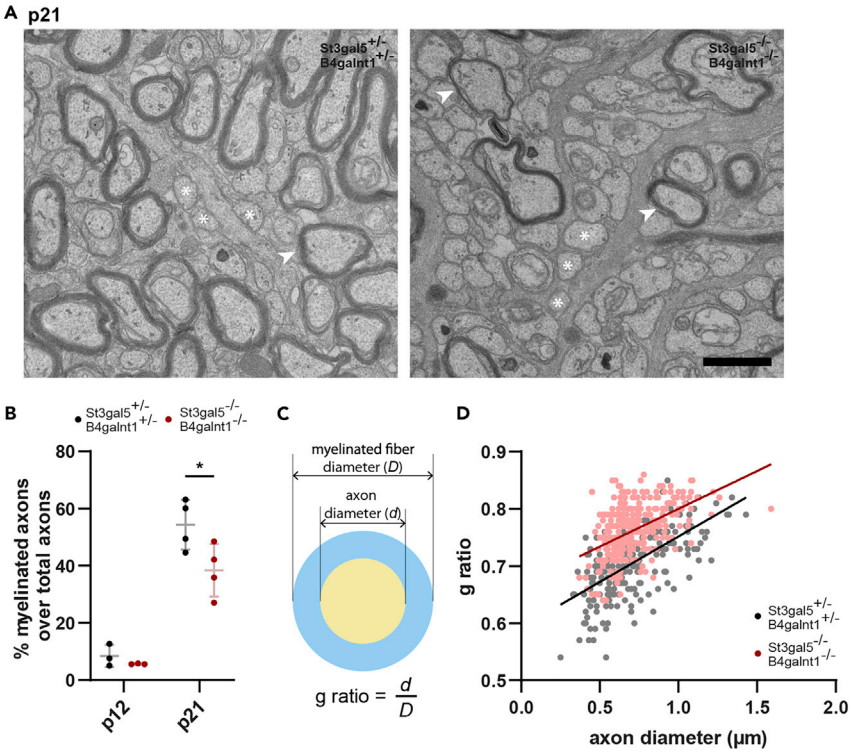


**Figure 6. Ultrastructural analysis of mouse optic nerves reveals hypomyelination in *St3gal5/B4galnt1*-deficient mice**

(A) Representative TEM images at p21 show less myelinated axons and thinner myelin sheath in *St3gal5*$^{-/-}$/*B4galnt1*$^{-/-}$ mice. Asterisks mark unmyelinated axons. Arrows show myelinated axons. Scale bar 5µm.

(B) Graph displays the percentage of myelinated axons over the total number of axons at p12 and p21. We did not detect differences at p12 (p = 0.279). At p21 *St3gal5*$^{-/-}$/*B4galnt1*$^{-/-}$ mice displayed significantly less myelinated axons (p = 0.045). Differences were tested with an unpaired t-test, two-tailed.

(C) G ratios are calculated by dividing the axonal diameter with the myelinated fiber diameter.

(D) Scatterplot displaying the g ratios of individual myelinated axons as a function of the respective axon caliber with simple linear regression at p21. *St3gal*$^{+/}$/*B4galnt*$^{+/-}$ slope = 0.15, *St3gal5*$^{-/-}$/*B4galnt1*$^{-/-}$ slope = 0.13. All values are represented as mean ± SD. Figure related to Figure S6.

have been proven to deliver impressive analytical performance regarding sensitivity, reproducibility, linearity, and even the resolution of isomeric lipid species, they are not suitable when available sample amounts are limited. Here, we describe and validate a shotgun lipidomics method for the analysis of gangliosides in tissue samples, which draws on established concepts for the analysis of gangliosides (Svennerholm and Fredman, 1980; Williams and McCluer, 1980) and extends them to overcome limitations of current methods. Most importantly, ganglioside analysis is performed from the remaining water phase of an established protocol for the analysis of global tissue lipidomes (Ejsing et al., 2009; Sampaio et al., 2011; Surma et al., 2021). This enables the simultaneous analysis of a highly diverse set of lipid classes from a single sample. More specifically, gangliosides are analyzed together with apolar lipids such as triglycerides and cholesterol esters, polar GPLs, as well as sphingolipids like sphingomyelin and ceramide from a single sample. Nevertheless, the required sample amounts are minimal: a few hundred µg of brain tissue is sufficient for the analysis of this diverse spectrum of lipids. Small amounts of sample result in low volumes of extraction solvents, which allows the use of SPE cartridges in a 96-well format, a requirement for the automatization of the protocol. SPE eluates are directly infused into the mass spectrometer using a robotic nano-electrospray ionization source, enabling analysis times of a maximum of 3 min per sample. Therefore, the method is ideally suited for the high throughput of large sample numbers. Yet, the analytical performance is comparable to that of LC-MS-based approaches (e.g. Fong et al., 2009): sensitivity is in the nM range, linearity is achieved over 4 orders of magnitude, and method precision is <15% when suitable internal lipid standards are available. The shotgun lipidomics analysis allows for the detection and quantification of the major

brain ganglioside classes: GM1, GD1, GT1, and GQ1 as well as intermediates of the ganglioside biosynthesis pathways, such as GM3 and GD3. The ganglioside class profiles obtained here are comparable to those reported for brain samples of mice and other species (Wormwood Moser et al., 2021; Ikeda and Taguchi, 2010; Hajek et al., 2017; Schnaar et al., 2014; Borgmeyer et al., 2021). Limitations of the method are the inability to resolve isomeric ganglioside species (such as GD1a vs GD1b) as well as the lack of suitable internal standards for several ganglioside classes. However, its compatibility with methods for global lipidomic profiling together with its high throughput capabilities will improve access of scientists from diverse areas of research to ganglioside analysis. The requirement for only minimal sample amounts (starting from 50 µg of tissue wet weight) will enable the quantification of gangliosides from fine anatomical structures, hopefully providing novel insights into the functions of this fascinating group of lipid molecules.

While the proteome composition of myelin and the myelin-axolemmal complex has been addressed (Menon et al., 2003; Taylor et al., 2004; Jahn et al., 2009; Dhaunchak et al., 2010; Mukherjee et al., 2020), we know little about its lipid composition. We applied our method to analyze the ganglioside content during development in the wild-type murine brain and optic nerve. In future, further brain regions and at different time points need to be analyzed. We observed a shift from simple to complex gangliosides during development not only regarding the complexity of the glycan head but also in the ceramide backbone, which is consistent with other studies (Kolter et al., 2002; Lahiri and Futerman, 2007; Russo et al., 2018). We detected simple ganglioside species mostly in the early and intermediate stages of myelination, whereas the complex ganglioside species are more abundant at intermediate and fully developed myelination stages. In addition, subspecies with longer carbon chains and two double bonds were found predominantly at stages when myelination is almost or fully completed. We did not find any LacCer at any age, possibly because LacCer is immediately synthesized into different ganglioside species.

Our lipidomic data of brain samples from P21 wild-type, *St3gal5/B4galnt1* double heterozygous, and *St3gal5/B4galnt1*-deficient mice confirm clearly that our approach reliably detects gangliosides differing in their number of carbons in fatty acid chains and double bonds. We confirmed the almost complete lack of gangliosides in the brain of *St3gal5/B4galnt1*-deficient mice. In line with a study from Yamashita et al., (2005), the lack of gangliosides is further supported by detection of high levels of LacCer, which serves as a precursor of all gangliosides. Nevertheless, we still detected signals of GD1, GM1, GD3, and GT1 in some of the brain samples from *St3gal5/B4galnt1*-deficient mice. As demonstrated by Yamashita et al., these signals are derived from sialylated neolacto-series glycosphingolipids. Previously, low levels of GD1a and GT1b were detected in St3gal2/3-deficient mice, suggesting that other St3gal enzymes might take over sialylation to replace the lacking gangliosides at least to a low extent (Sturgill et al., 2012).

To our surprise, the general lipid composition of *St3gal5/B4galnt1* double heterozygous and *St3gal5/B4galnt1*-deficient mice does not differ significantly from that of wild-type animals. In order to investigate how these animals compensate for the lack of gangliosides, we analyzed the length of the carbon chains and their saturation. As a compensatory mechanism for a lack of gangliosides, we expected to find an increase in longer and more saturated carbon chains in other lipid classes. However, in *St3gal5/B4galnt1* double heterozygous and *St3gal5/B4galnt1*-deficient mice, the average length and saturation of the carbon chains in other lipid classes hardly changed.

We also examined the role of gangliosides in axon-myelin interactions by ultrastructural analysis. Surprisingly, our ultrastructural analysis revealed only subtle deficits in myelination of the optic nerve of St3gal5/B4galnt1-deficient mice only at P21. We detected myelin of normal ultrastructure but slightly thinner myelin sheaths and disorganized paranodes, which is not consistent with previous findings (Yamashita et al., 2005). Thus, the white matter vacuolization profiles observed previously in 1.5- to 3-month-old *St3gal5/B4galnt1*-deficient mice (Yamashita et al., 2005) and the impairment of neurological function are most likely a result of defective maintenance and/or increased degeneration.

In summary, we developed a quantitative mass-spectrometry-based shotgun lipidomics method for the analysis of gangliosides and showed its relevance for studies of neurological function. The compatibility

of our shotgun method with global lipidomic profiling methods will technically open up an area of research, which has so far been unreachable.

### Limitations of the study

Limitations of our study include lack of standards for most ganglioside species and lack of detection of some gangliosides due to low sensitivity. In addition, more brain regions and time points need to be studied to resolve the brain ganglioside lipidome more comprehensively.

## STAR★METHODS

Detailed methods are provided in the online version of this paper and include the following:

- KEY RESOURCES TABLE
- RESOURCE AVAILABILITY
  - Lead contact
  - Materials availability
  - Data and code availability
- EXPERIMENTAL MODEL AND SUBJECT DETAILS
  - Mice
- METHOD DETAILS
  - Transmission electron microscopy
  - Tissue preparation for lipidomics
  - Annotation of lipid classes and species
  - Lipid standard titration
  - Lipid extraction for mass spectrometry lipidomics
  - MS data acquisition
  - Lipidomic analysis of gangliosides
- QUANTIFICATION AND STATISTICAL ANALYSIS
  - Data analysis and post-processing
  - Electron microscopy analysis

## SUPPLEMENTAL INFORMATION

Supplemental information can be found online at https://doi.org/10.1016/j.isci.2022.105323.

## ACKNOWLEDGMENTS

The work was supported by grants from the German Research Foundation (ID 408885537-TRR 274, TRR128, ERC-ADG (101019594), SyNergy Excellence Cluster (EXC 2145, Projekt ID390857198), the Human Frontier Science Program (HFSP), and the BMBF through the projects CLINSPECT-M. The graphical abstract and Figure 1 were created with BioRender.com. We would like to thank Kerstin Karg for the technical assistance with sample preparation for EM analysis.

## AUTHOR CONTRIBUTIONS

M.S. and C.K. conceived the project and designed experiments. M.A., M.W., C.P., M.D., M.A.S., C.S., and C.K. carried out experiments. M.A., M.W., C.P., M.D., M.A.S., C.S., C.K, L.J., and M.S. analyzed the data or supervised data acquisition. L.C. and S.L. provided essential reagents. M.A. and C.K. visualized the data. M.A., C.K., and M.S. wrote the manuscript.

## DECLARATION OF INTERESTS

Christian Klose and Michal A Surma are shareholders of Lipo-type GmbH. Melanie Weber, Cyrus Papan, and Markus Damm are employees of Lipo-type GmbH. Shengrong Li and Lisa Connell are employees of Avanti Lipids.

Received: June 7, 2022
Revised: August 2, 2022
Accepted: October 7, 2022
Published: November 18, 2022

## REFERENCES

Bakhti, M., Snaidero, N., Schneider, D., Aggarwal, S., Mobius, W., Janshoff, A., Eckhardt, M., Nave, K.A., and Simons, M. (2013). Loss of electrostatic cell-surface repulsion mediates myelin membrane adhesion and compaction in the central nervous system. Proc. Natl. Acad. Sci. USA *110*, 3143–3148.

Barrientos, R.C., and Zhang, Q. (2020). Recent advances in the mass spectrometric analysis of glycosphingolipidome — a review. Anal. Chim. Acta *1132*, 134–155.

Borgmeyer, M., Coman, C., Has, C., Schott, H.F., Li, T., Westhoff, P., Cheung, Y.F.H., Hoffmann, N., Yuanxiang, P., Behnisch, T., et al. (2021). Multiomics of synaptic junctions reveals altered lipid metabolism and signaling following environmental enrichment. Cell Rep. *37*, 109797.

Collins, B.E., Ito, H., Sawada, N., Ishida, H., Kiso, M., and Schnaar, R.L. (1999). Enhanced binding of the neural siglecs, myelin-associated glycoprotein and Schwann cell myelin protein, to Chol-1 (alpha-series) gangliosides and novel sulfated Chol-1 analogs. J. Biol. Chem. *274*, 37637–37643.

Collins, B.E., Yang, L.J., Mukhopadhyay, G., Filbin, M.T., Kiso, M., Hasegawa, A., and Schnaar, R.L. (1997). Sialic acid specificity of myelin-associated glycoprotein binding. J. Biol. Chem. *272*, 1248–1255.

Desplats, P.A., Denny, C.A., Kass, K.E., Gilmartin, T., Head, S.R., Sutcliffe, J.G., Seyfried, T.N., and Thomas, E.A. (2007). Glycolipid and ganglioside metabolism imbalances in Huntington's disease. Neurobiol. Dis. *27*, 265–277.

Dhaunchak, A.S., Huang, J.K., De Faria Junior, O., Roth, A.D., Pedraza, L., Antel, J.P., Bar-Or, A., and Colman, D.R. (2010). A proteome map of axoglial specializations isolated and purified from human central nervous system. Glia *58*, 1949–1960.

Djannatian, M., Timmler, S., Arends, M., Luckner, M., Weil, M.T., Alexopoulos, I., Snaidero, N., Schmid, B., Misgeld, T., Mobius, W., et al. (2019). Two adhesive systems cooperatively regulate axon ensheathment and myelin growth in the CNS. Nat. Commun. *10*, 4794.

Ejsing, C.S., Sampaio, J.L., Surendranath, V., Duchoslav, E., Ekroos, K., Klemm, R.W., Simons, K., and Shevchenko, A. (2009). Global analysis of the yeast lipidome by quantitative shotgun mass spectrometry. Proc. Natl. Acad. Sci. USA *106*, 2136–2141.

Fong, B., Norris, C., Lowe, E., and McJarrow, P. (2009). Liquid chromatography-high-resolution mass spectrometry for quantitative analysis of gangliosides. Lipids *44*, 867–874.

Futerman, A.H., and Pagano, R.E. (1991). Determination of the intracellular sites and topology of glucosylceramide synthesis in rat liver. Biochem. J. *280*, 295–302.

Hajek, R., Jirasko, R., Lisa, M., Cifkova, E., and Holcapek, M. (2017). Hydrophilic interaction liquid chromatography-mass spectrometry characterization of gangliosides in biological samples. Anal. Chem. *89*, 12425–12432.

Herzog, R., Schuhmann, K., Schwudke, D., Sampaio, J.L., Bornstein, S.R., Schroeder, M., and Shevchenko, A. (2012). LipidXplorer: a software for consensual cross-platform lipidomics. PLoS One *7*, e29851.

Herzog, R., Schwudke, D., Schuhmann, K., Sampaio, J.L., Bornstein, S.R., Schroeder, M., and Shevchenko, A. (2011). A novel informatics concept for high-throughput shotgun lipidomics based on the molecular fragmentation query language. Genome Biol. *12*, R8.

Hirschberg, K., Rodger, J., and Futerman, A.H. (1993). The long-chain sphingoid base of sphingolipids is acylated at the cytosolic surface of the endoplasmic reticulum in rat liver. Biochem. J. *290*, 751–757.

Horejsi, K., Jirasko, R., Chocholouskova, M., Wolrab, D., Kahoun, D., and Holcapek, M. (2021). Comprehensive identification of glycosphingolipids in human plasma using hydrophilic interaction liquid chromatography-electrospray ionization mass spectrometry. Metabolites *11*.

Ikeda, K., Shimizu, T., and Taguchi, R. (2008). Targeted analysis of ganglioside and sulfatide molecular species by LC/ESI-MS/MS with theoretically expanded multiple reaction monitoring. J. Lipid Res. *49*, 2678–2689.

Ikeda, K., and Taguchi, R. (2010). Highly sensitive localization analysis of gangliosides and sulfatides including structural isomers in mouse cerebellum sections by combination of laser microdissection and hydrophilic interaction liquid chromatography/electrospray ionization mass spectrometry with theoretically expanded multiple reaction monitoring. Rapid Commun. Mass Spectrom. *24*, 2957–2965.

Irwin, L.N., Michael, D.B., and Irwin, C.C. (1980). Ganglioside patterns of fetal rat and mouse brain. J. Neurochem. *34*, 1527–1530.

Jahn, O., Tenzer, S., and Werner, H.B. (2009). Myelin proteomics: molecular anatomy of an insulating sheath. Mol. Neurobiol. *40*, 55–72.

Kolter, T., Proia, R.L., and Sandhoff, K. (2002). Combinatorial ganglioside biosynthesis. J. Biol. Chem. *277*, 25859–25862.

Lahiri, S., and Futerman, A.H. (2007). The metabolism and function of sphingolipids and glycosphingolipids. Cell. Mol. Life Sci. *64*, 2270–2284.

Liebisch, G., Binder, M., Schifferer, R., Langmann, T., Schulz, B., and Schmitz, G. (2006). High throughput quantification of cholesterol and cholesteryl ester by electrospray ionization tandem mass spectrometry (ESI-MS/MS). Biochim. Biophys. Acta *1761*, 121–128.

Liu, Y., Wada, R., Kawai, H., Sango, K., Deng, C., Tai, T., McDonald, M.P., Araujo, K., Crawley, J.N., Bierfreund, U., et al. (1999). A genetic model of substrate deprivation therapy for a glycosphingolipid storage disorder. J. Clin. Invest. *103*, 497–505.

Ma, Q., Kobayashi, M., Sugiura, M., Ozaki, N., Nishio, K., Shiraishi, Y., Furukawa, K., Furukawa, K., and Sugiura, Y. (2003). Morphological study of disordered myelination and the degeneration of nerve fibers in the spinal cord of mice lacking complex gangliosides. Arch. Histol. Cytol. *66*, 37–44.

McGonigal, R., Barrie, J.A., Yao, D., McLaughlin, M., Cunningham, M.E., Rowan, E.G., and Willison, H.J. (2019). Glial sulfatides and neuronal complex gangliosides are functionally interdependent in maintaining myelinating axon integrity. J. Neurosci. *39*, 63–77.

Menon, K., Rasband, M.N., Taylor, C.M., Brophy, P., Bansal, R., and Pfeiffer, S.E. (2003). The myelin-axolemmal complex: biochemical dissection and the role of galactosphingolipids. J. Neurochem. *87*, 995–1009.

Molander, M., Berthold, C.H., Persson, H., and Fredman, P. (2000). Immunostaining of ganglioside GD1b, GD3 and GM1 in rat cerebellum: cellular layer and cell type specific associations. J. Neurosci. Res. *60*, 531–542.

Mukherjee, C., Kling, T., Russo, B., Miebach, K., Kess, E., Schifferer, M., Pedro, L.D., Weikert, U., Fard, M.K., Kannaiyan, N., et al. (2020). Oligodendrocytes provide antioxidant defense function for neurons by secreting ferritin heavy chain. Cell Metabol. *32*, 259–272.

Nawaz, S., Sanchez, P., Schmitt, S., Snaidero, N., Mitkovski, M., Velte, C., Bruckner, B.R., Alexopoulos, I., Czopka, T., Jung, S.Y., et al. (2015). Actin filament turnover drives leading edge growth during myelin sheath formation in the central nervous system. Dev. Cell *34*, 139–151.

Olsen, A.S.B., and Faergeman, N.J. (2017). Sphingolipids: membrane microdomains in brain development, function and neurological diseases. Open Biol. *7*.

Panzenboeck, L., Troppmair, N., Schlachter, S., Koellensperger, G., Hartler, J., and Rampler, E. (2020). Chasing the major sphingolipids on earth: automated annotation of plant glycosyl inositol phospho ceramides by glycolipidomics. Metabolites *10*.

Pronker, M.F., Lemstra, S., Snijder, J., Heck, A.J., Thies-Weesie, D.M., Pasterkamp, R.J., and Janssen, B.J. (2016). Structural basis of myelin-associated glycoprotein adhesion and signalling. Nat. Commun. *7*, 13584.

Rasband, M.N., and Peles, E. (2015). The nodes of ranvier: molecular assembly and maintenance. Cold Spring Harbor Perspect. Biol. *8*, a020495.

Russo, D., Capolupo, L., Loomba, J.S., Sticco, L., and D'Angelo, G. (2018). Glycosphingolipid metabolism in cell fate specification. J. Cell Sci. *131*.

Sampaio, J.L., Gerl, M.J., Klose, C., Ejsing, C.S., Beug, H., Simons, K., and Shevchenko, A. (2011). Membrane lipidome of an epithelial cell line. Proc. Natl. Acad. Sci. USA *108*, 1903–1907.

Schnaar, R.L., Gerardy-Schahn, R., and Hildebrandt, H. (2014). Sialic acids in the brain: gangliosides and polysialic acid in nervous system development, stability, disease, and regeneration. Physiol. Rev. *94*, 461–518.

Sheikh, K.A., Sun, J., Liu, Y., Kawai, H., Crawford, T.O., Proia, R.L., Griffin, J.W., and Schnaar, R.L. (1999). Mice lacking complex gangliosides develop Wallerian degeneration and myelination defects. Proc. Natl. Acad. Sci. USA *96*, 7532–7537.

Simons, M., and Nave, K.A. (2015). Oligodendrocytes: myelination and axonal support. Cold Spring Harbor Perspect. Biol. *8*, a020479.

Snaidero, N., Mobius, W., Czopka, T., Hekking, L.H., Mathisen, C., Verkleij, D., Goebbels, S., Edgar, J., Merkler, D., Lyons, D.A., et al. (2014). Myelin membrane wrapping of CNS axons by PI(3,4,5)P3-dependent polarized growth at the inner tongue. Cell *156*, 277–290.

Stadelmann, C., Timmler, S., Barrantes-Freer, A., and Simons, M. (2019). Myelin in the central nervous system: structure, function, and pathology. Physiol. Rev. *99*, 1381–1431.

Sturgill, E.R., Aoki, K., Lopez, P.H., Colacurcio, D., Vajn, K., Lorenzini, I., Majic, S., Yang, W.H., Heffer, M., Tiemeyer, M., et al. (2012). Biosynthesis of the major brain gangliosides GD1a and GT1b. Glycobiology *22*, 1289–1301.

Surma, M.A., Gerl, M.J., Herzog, R., Helppi, J., Simons, K., and Klose, C. (2021). Mouse lipidomics reveals inherent flexibility of a mammalian lipidome. Sci. Rep. *11*, 19364.

Surma, M.A., Herzog, R., Vasilj, A., Klose, C., Christinat, N., Morin-Rivron, D., Simons, K., Masoodi, M., and Sampaio, J.L. (2015). An automated shotgun lipidomics platform for high throughput, comprehensive, and quantitative analysis of blood plasma intact lipids. Eur. J. Lipid Sci. Technol. *117*, 1540–1549.

Susuki, K., Baba, H., Tohyama, K., Kanai, K., Kuwabara, S., Hirata, K., Furukawa, K., Furukawa, K., Rasband, M.N., and Yuki, N. (2007). Gangliosides contribute to stability of paranodal junctions and ion channel clusters in myelinated nerve fibers. Glia *55*, 746–757.

Svennerholm, L., and Fredman, P. (1980). A procedure for the quantitative isolation of brain gangliosides. Biochim. Biophys. Acta *617*, 97–109.

Takamiya, K., Yamamoto, A., Furukawa, K., Yamashiro, S., Shin, M., Okada, M., Fukumoto, S., Haraguchi, M., Takeda, N., Fujimura, K., et al. (1996). Mice with disrupted GM2/GD2 synthase gene lack complex gangliosides but exhibit only subtle defects in their nervous system. Proc. Natl. Acad. Sci. USA *93*, 10662–10667.

Taylor, C.M., Marta, C.B., Claycomb, R.J., Han, D.K., Rasband, M.N., Coetzee, T., and Pfeiffer, S.E. (2004). Proteomic mapping provides powerful insights into functional myelin biology. Proc. Natl. Acad. Sci. USA *101*, 4643–4648.

Vajn, K., Viljetic, B., Degmecic, I.V., Schnaar, R.L., and Heffer, M. (2013). Differential distribution of major brain gangliosides in the adult mouse central nervous system. PLoS One *8*, e75720.

Williams, M.A., and McCluer, R.H. (1980). The use of Sep-Pak C18 cartridges during the isolation of gangliosides. J. Neurochem. *35*, 266–269.

Wormwood Moser, K.L., Van Aken, G., DeBord, D., Hatcher, N.G., Maxon, L., Sherman, M., Yao, L., and Ekroos, K. (2021). High-defined quantitative snapshots of the ganglioside lipidome using high resolution ion mobility SLIM assisted shotgun lipidomics. Anal. Chim. Acta *1146*, 77–87.

Yamashita, T., Hashiramoto, A., Haluzik, M., Mizukami, H., Beck, S., Norton, A., Kono, M., Tsuji, S., Daniotti, J.L., Werth, N., et al. (2003). Enhanced insulin sensitivity in mice lacking ganglioside GM3. Proc. Natl. Acad. Sci. USA *100*, 3445–3449.

Yamashita, T., Wu, Y.P., Sandhoff, R., Werth, N., Mizukami, H., Ellis, J.M., Dupree, J.L., Geyer, R., Sandhoff, K., and Proia, R.L. (2005). Interruption of ganglioside synthesis produces central nervous system degeneration and altered axon-glial interactions. Proc. Natl. Acad. Sci. USA *102*, 2725–2730.

Yang, L.J., Zeller, C.B., Shaper, N.L., Kiso, M., Hasegawa, A., Shapiro, R.E., and Schnaar, R.L. (1996). Gangliosides are neuronal ligands for myelin-associated glycoprotein. Proc. Natl. Acad. Sci. USA *93*, 814–818.

Yoshikawa, M., Go, S., Takasaki, K., Kakazu, Y., Ohashi, M., Nagafuku, M., Kabayama, K., Sekimoto, J., Suzuki, S., Takaiwa, K., et al. (2009). Mice lacking ganglioside GM3 synthase exhibit complete hearing loss due to selective degeneration of the organ of Corti. Proc. Natl. Acad. Sci. USA *106*, 9483–9488.

Yu, R.K., Macala, L.J., Taki, T., Weinfield, H.M., and Yu, F.S. (1988). Developmental changes in ganglioside composition and synthesis in embryonic rat brain. J. Neurochem. *50*, 1825–1829.

Zuchero, J.B., Fu, M.M., Sloan, S.A., Ibrahim, A., Olson, A., Zaremba, A., Dugas, J.C., Wienbar, S., Caprariello, A.V., Kantor, C., et al. (2015). CNS myelin wrapping is driven by actin disassembly. Dev. Cell *34*, 152–167.

## STAR★METHODS

### KEY RESOURCES TABLE

| REAGENT or RESOURCE | SOURCE | IDENTIFIER |
|---|---|---|
| Experimental models: Organisms/strains | | |
| Mouse: B6;129S-St3gal5$^{tm1Rlp}$/Mmmh | MMRRC | 000374-MU |
| Mouse: B6;129S-B4galnt1$^{tm1Rlp}$/Mmmh | MMRRC | 000036-MU |
| Chemicals, peptides, and recombinant proteins | | |
| C18:0 GM1-d3 | Matreya LLC | 2050 |
| C18:0 GM3-d3 | Matreya LLC | 2052 |
| Deposited data | | |
| Lipidomic data | This Manuscript | See Table S3 |
| Software and algorithms | | |
| LipidXplorer | Herzog et al., 2011, 2012 | Lipo-type GmbH |
| Adobe Illustrator CS5 | Adobe Systems Software Ireland Limited | https://www.adobe.com/de/products/ |
| GraphPad Prism 9 | Graphpad Software, Inc. | https://www.graphpad.com/ |
| BioRender | | https://biorender.com/ |
| Other | | |
| Tenbroeck Tissue Grinders, 1 mL or 2 mL | VWR | 432 -1275; 1276 |
| QExactive mass spectrometer | Thermo Scientific | https://www.thermofisher.com/us/en/home.html |
| TriVersa NanoMate ion source | Advion Biosciences | https://www.advion.com |

### RESOURCE AVAILABILITY

#### Lead contact

Further information and requests for resources and reagents should be directed to and will be fulfilled by the lead contact, Mikael Simons (mikael.Simons@dzne.de).

#### Materials availability

This study did not generate unique reagents.

#### Data and code availability

- The lipidomics datasets are provided in Table S3.
- This study did not generate any code.
- Any additional information required to reanalyze the data reported in this paper is available from the lead contact upon request.

### EXPERIMENTAL MODEL AND SUBJECT DETAILS

#### Mice

Mice were group-housed under pathogen-free conditions and bred in the animal housing facility of the Center of Stroke and Dementia Research or the Institute of Neuronal Cell Biology, Technical University Munich. All experiments were carried out in compliance with the National Guidelines for Animal Protection, Germany, with the approval of the regional Animal care committee of the Government of Upper Bavaria (project license AZ55.2-1-54-2532-157). Double mutant mice (St3gal5$^{-/-}$/B4galnt1$^{-/-}$) were generated by KO/het crossbreeding of male St3gal5$^{-/-}$/B4galnt1$^{+/-}$ x female St3gal5$^{+/-}$B4galnt1$^{-/-}$ as male B4galnt1$^{-/-}$ are sterile (Liu et al., 1999). Litters with potential double mutant animals were monitored for their burden every second day from P8 until P12 or P21, respectively. Male and female mice were used for the study.

## METHOD DETAILS

### Transmission electron microscopy

Mouse optic nerves were prepared after deep anesthesia (isoflurane) perfusion fixation and immersion fixed (2.5% glutaraldehyde and 4% paraformaldehyde in 0.1 M sodium cacodylate buffer at pH 7.4.) for 24 h at 4°C. After tissue trimming and washes in 0.1 M sodium cacodylate buffer, postfixation in reduced osmium (2% osmium, 2.5% potassium ferrocyanide in 0.1 M cacodylate buffer) was followed by *en bloc* uranyl acetate (1% aqueous uranylacetate) contrasting, graded dehydration in ethanol and embedding in epon resin (Serva). After ultrathin sectioning the grids (Leica UC7 ultramicrotome) were contrasted by 1% uranyl acetate and Ultrostain (Leica). Images were acquired with a JEOL JEM1400 plus TEM equipped with a Ruby 8 Mpx CCD camera.

### Tissue preparation for lipidomics

Mouse optic nerves were prepared after deep anesthesia (isoflurane) perfusion with D-PBS without $Mg^{+}$ and $Ca^{2+}$ (Gibco) only. This step was necessary to remove circulating blood cells from the brain and thus prevent contamination of our samples. No fixative was applied afterward. Samples were kept on ice whenever possible. After weighing and pooling (p12: 3-4 ON, p21: 2-3 ON, adult:1-2 ON) to reach a minimum concentration of 5 mg/mL tissue, brains and optic nerves were homogenized on ice using a 1 mL or 2 mL Tenbroeck glass tissue homogenizer (VWR). Samples were stored in D-PBS without $Mg^{+}$ and $Ca^{2+}$ in 1 mL or 2 mL Eppendorf tubes at −80°C in 2.0 mL Eppendorf Safe-Lock Tubes in until shipment.

### Annotation of lipid classes and species

Glycerolipids are referred to as triacylglycerols (TAG) and diacylglycerols (DAG); glycerophospholipids and lyso-glycerophospholipids to phosphatidic acids (PA), phosphatidylinositols (PI), phosphatidylserines (PS), phosphatidylglycerols (PG), phosphatidylethanolamines (PE), phosphatidylcholines (PC), ether phosphatidylethanolamines (PE O-), ether phosphatidylcholines (PC O-), lysophosphatidic acids (LPA), lyso-phosphatidylinositols (LPI), lyso-phosphatidylcholines (LPC), and lyso-phosphatidylethanolamines (LPE); sphingolipids to ceramides (Cer) and sphingomyelins (SM); sterols to cholesterol (Chol) and cholesterylesters (CE). Lipid species are annotated according to their molecular composition as follows: [lipid class]-[sum of carbon atoms in LCB and FAs]:[sum of double bonds in LCB and FAs]; [sum of hydroxyl groups in LCB and FA] (e.g., SM 36:1; 2 denotes sphingomyelin with a total length of its LCB and FA of 36; with 1 double bonds and 2 hydroxylations in total). For lipid subspecies, the individual acyl chain composition according to the same rule is given (e.g., 18:1; 0_24:2; 0), with the first entity denoting a sphingoid base (LCB) and the second a fatty acid (FA), in case of ceramides. Ceramides naming convention was adopted from Surma et al. (2015).

### Lipid standard titration

For the assessment of sensitivity and linearity of the ganglioside analysis, lipid references were purchased from Matreya (Matreya LLC) or Avanti (Avanti Polar Lipids, Inc.). Because these are natural ganglioside extracts, they contain a multitude individual lipid species. For use in the assessment of sensitivity and linearity, the fraction of the most abundant species was determined by direct infusion mass spectrometry and the concentration calculated based on the total concentration of the ganglioside mixture. The concentration and intensity values of the most abundant lipid species in the mixture was used for calculation of limit of detection and limit of quantification.

### Lipid extraction for mass spectrometry lipidomics

Mass spectrometry-based lipid analysis was performed by Lipo-type GmbH (Dresden, Germany) as described (Surma et al., 2021). If not indicated otherwise, 500 µg of tissue were used per extraction. Lipids were extracted using a two-step chloroform/methanol procedure using homogenized tissues re-suspended in a water phase, extracted with chloroform/methanol 10:1 (V:V) and 2:1 (V:V) in the first and second step, respectively (Ejsing et al., 2009). Samples were spiked with internal lipid standard mixture containing: cardiolipin 16:1/15:0/15:0/15:0 (CL, 50 pmol per extraction), ceramide 18:1; 2/17:0 (Cer, 30 pmol), diacylglycerol 17:0/17:0 (DAG, 100 pmol), hexosylceramide 18:1; 2/12:0 (HexCer, 30 pmol), lyso-phosphatidate 17:0 (LPA, 30 pmol), lyso-phosphatidylcholine 12:0 (LPC, 50 pmol), lyso-phosphatidylethanolamine 17:1 (LPE, 30 pmol), lyso-phosphatidylglycerol 17:1 (LPG, 30 pmol), lyso-phosphatidylinositol 17:1 (LPI, 20 pmol), lyso-phosphatidylserine 17:1 (LPS, 30 pmol), phosphatidate 17:0/17:0 (PA, 50 pmol), phosphatidylcholine 17:0/17:0 (PC, 150 pmol), phosphatidylethanolamine 17:0/17:0 (PE, 75 pmol), phosphatidylglycerol 17:0/17:0 (PG, 50 pmol), phosphatidylinositol 16:0/16:0 (PI, 50 pmol), phosphatidylserine 17:0/17:0 (PS, 100

pmol), cholesterol ester 20:0 (CE, 100 pmol), sphingomyelin 18:1; 2/12:0; 0 (SM, 50 pmol), triacylglycerol 17:0/17:0/17:0 (TAG, 75 pmol), Gb3 18:1; 2/17:0; 0 (200 pmol), GM1-D3 18:1; 2/18:0; 0 (200 pmol), GM3-D3 18:1; 2/18:0; 0 (50 pmol), LacCer d18:1/12:0 (50 pmol), Sulfatide d18:1; 2/12:0; 0 (20 pmol) and cholesterol D6 (Chol, 300 pmol). After extraction, the organic phase was transferred to an infusion plate and dried in a speed vacuum concentrator. 1st step dry extract was re-suspended in 7.5 mM ammonium acetate in chloroform/methanol/propanol (1:2:4, V:V:V) and 2nd step dry extract in 33% ethanol solution of methylamine in chloroform/methanol (0.003:5:1; V:V:V). All liquid handling steps were performed using Hamilton Robotics STARlet robotic platform with the Anti Droplet Control feature for organic solvents pipetting.

### MS data acquisition

Samples were analyzed by direct infusion on a QExactive mass spectrometer (Thermo Scientific) equipped with a Tri-Versa NanoMate ion source (Advion Biosciences). Samples were analyzed in both positive and negative ion modes with a resolution of $R_{m/z=200}$ = 280,000 for MS and $R_{m/z=200}$ = 17,500 for MSMS experiments, in a single acquisition. MSMS was triggered by an inclusion list encompassing corresponding MS mass ranges scanned in 1 Da increments with normalized collision energies of 20 and 35% for positively and negatively charged ions, respectively (Surma et al., 2015). Both MS and MSMS data were combined to monitor CE, DAG and TAG ions as ammonium adducts; PC, PC O-, as acetate adducts; and CL, PA, PE, PE O-, PG, PI and PS as deprotonated anions. MS only was used to monitor LPA, LPE, LPE O-, LPI, LPS, GM2, GM3, GM4, and Gb3 as deprotonated anions; Cer, HexCer, SM, LPC and LPC O-as acetate adducts and cholesterol as ammonium adduct of an acetylated derivative (Liebisch et al., 2006). To control for technical variation, background signals and sample carry-over, a total of 6 blank and 6 reference samples included in the analytical run and distributed evenly across the sample set, resulting in a blank and reference sample after every seventh study sample.

### Lipidomic analysis of gangliosides

The gangliosides GM2, GM3, GM4 were analyzed in the chloroform/methanol 2:1 (V:V) fraction, the second step of the two-step chloroform/methanol extraction procedure. Ganglioside classes GM1, GD1, GD2, GD3, GT1, GT2, GT3, GQ1 were extracted from the remaining water phase of the second step. They were then subjected to purification using solid phase extraction (Thermo Scientific SOLA SPE plates, 10 mg/2 mL). The water phase was loaded on columns pre-washed with chloroform/methanol (2:1, V:V), methanol and methanol/water (1:1, V:V); with the input flow through re-applied three times. Then, columns were washed with water and the elution was carried out two times with methanol and one time with chloroform/methanol (1:1, V:V). Washing and elution steps were carried using a vacuum manifold. Pooled eluates were dried in a speed vacuum concentrator and re-suspended in 33% ethanol solution of methylamine in chloroform/methanol (0.003:5:1; V:V:V). Ganglioside extracts were analyzed by direct infusion on a QExactive mass spectrometer (Thermo Scientific) equipped with a Tri-Versa NanoMate ion source (Advion Biosciences). Sample infusion was performed with a pressure p = 0.8 psi and voltage V = 0.95 V. Samples were analyzed in negative ion modes with a resolution of $R_{m/z=200}$ = 140,000; AGC target of $1 \times 10^6$; maximum injection time of 500 ms and 3 microscans and a normalized collision energy of 30% for MSMS experiments at a resolution of $R_{m/z=200}$ = 17,500.

## QUANTIFICATION AND STATISTICAL ANALYSIS

### Data analysis and post-processing

Data were analyzed with in-house developed lipid identification software based on LipidXplorer (Herzog et al., 2011, 2012). Data post-processing and normalization were performed using an in-house developed data management system. Only lipid identifications with a signal-to-noise ratio >5, and a signal intensity 5-fold higher than in corresponding blank samples were considered for further data analysis. Lipids were normalized to lipid class-specific internal standards. In case of ganglioside classes for which no suitable lipid class-specific internal standards are available, spectral intensities were normalized to the internal standard GM1-D3 18:1; 2/18:0; 0 and the normalised intensities further normalised to total lipid content (in pmol) of the sample.

Only results with >1.5-fold change and a p value < 0.05 were selected from the web browser-based data visualization tool (LipotypeZoom) for levels of lipid species as the percentage of the total lipid amount for each sample.

Statistical analysis was performed using GraphPad Prism 8.4.3 (GraphPad Software, Inc.). To compare the interactions between different genotypes or developmental stages, two-way ANOVA followed by Tukey's post hoc test was used. A p value of $<0.05$ was considered significant in all tests. All values are represented as mean $\pm$ SD.

### Electron microscopy analysis

Simple linear regression was applied on g-ratio data. All data were tested for normal distribution. To estimate the number of myelinated and unmyelinated axons in optic nerves, 3 random areas (35 × 35μm) per animal of 3-4 animals were counted and the means were taken. Differences in the number of myelinated axons were tested with unpaired t test. Differences in paranodal structure between genotypes were tested using unpaired t test with Welch's correction or Mann-Whitney test.